Chemical Science

ROYAL SOCIETY OF CHEMISTRY

EDGE ARTICLE

View Article Online
View Journal

Cite this: DOI: 10.1039/d5sc09133k

All publication charges for this article have been paid for by the Royal Society of Chemistry

Beyond active sites: interfacial water engineering with single-atom Ni-WC_x for concurrent energy storage and biomass conversion

Xiaoyang He,[a] Dengke Xiong,[a] Kaiyan Zhang,[b] Wei Wang,[a] Shujie Xue,[a] Jianying Wang,*[a] Deli Wu[c] and Zuofeng Chen*[a]

Received 22nd November 2025
Accepted 24th December 2025

DOI: 10.1039/d5sc09133k

rsc.li/chemical-science

Coupling biomass valorization with rechargeable metal–air batteries offers a promising strategy to address energy storage and sustainable synthesis challenges. However, it demands highly active bifunctional catalysts capable of replacing the sluggish oxygen evolution reaction (OER) with value-added biomass electrooxidation. We report here a single-atom nickel-decorated tungsten carbide (Ni-WC_x) catalyst that demonstrates exceptional bifunctional activity for both the oxidation of 5-hydroxymethylfurfural (HMF) and the oxygen reduction reaction (ORR). The catalyst achieves near-quantitative conversion of HMF to furandicarboxylic acid (FDCA) with 99% selectivity and shows excellent ORR performance, featuring a half-wave potential ($E_{1/2}$) of 0.855 V. Through *in situ* spectroscopic analysis and multiscale simulations, we reveal a dual role of the atomically dispersed $Ni^{\delta+}$ sites: serving as intrinsic active centers and reconstructing the interfacial hydrogen-bond network to facilitate mass transport of bulky HMF molecules. When applied in an HMF-assisted Zn–air battery, the catalyst enables an ultralow charge–discharge voltage gap of 0.71 V at 20 mA cm^{-2} and remarkable cycling stability. This work proposes a new design strategy for electrocatalysts, emphasizing interfacial solvent engineering as a critical route to advanced hybrid energy-chemical systems.

Introduction

The integration of sustainable energy storage with green chemical synthesis represents an important research frontier.[1] A promising strategy to address these dual challenges involves replacing the sluggish oxygen evolution reaction (OER) in rechargeable zinc–air batteries (rZABs) with value-added electrocatalytic reactions, such as the oxidation of biomass-derived platform chemicals.[2] Among these, 5-hydroxymethylfurfural (HMF) is particularly noteworthy. Its conversion to 2,5-furandicarboxylic acid (FDCA) offers significant appeal, as FDCA serves as a high-value monomer for synthesizing polyethylene furanoate (PEF), a biodegradable alternative to petroleum-based polyethylene terephthalate (PET).[3–5] Coupling the HMF oxidation reaction (HMFOR) with the oxygen reduction reaction (ORR) in a hybrid rZAB system provides dual benefits: reducing the charging overpotential to enhance energy efficiency, while simultaneously enabling sustainable production of valuable chemicals.[6] However, the practical implementation of this technology hinges on the development of highly active, stable, and cost-effective bifunctional electrocatalysts capable of efficiently driving both HMFOR and ORR.[7]

Electrocatalysis is fundamentally governed by interfacial phenomena, involving complex interactions at both solid-state (metal–support) and solid–liquid (catalyst–electrolyte) interfaces.[8,9] At the solid-state level, constructing a stable and electronically coupled metal–support interface is essential. Single-atom catalysts (SACs) provide exceptional activity due to the unsaturated coordination sites and distinct electronic properties, yet their practical catalytic performance is highly dependent on the choice of support material.[10,11] While conventional N-doped carbon supports often suffer from insufficient stability due to weak anchoring of single atoms, tungsten carbide (WC_x) offers a robust and electronically active alternative. Its Pt-like d-band electronic structure, high electrical conductivity, and replaceable lattice atoms promote efficient charge transfer and strong metal–support interactions, creating an ideal platform for stabilizing single atoms and enhancing their intrinsic activity.[12] Furthermore, dopant–substrate interaction can modulate the electronic structure of WC_x, thereby boosting the intrinsic activity of the substrate.

Beyond the solid-state interface, interfacial solvent structures play a critical role in diffusion-limited reactions such as

[a]School of Chemical Science and Engineering, Tongji University, 1239 Siping Road, Shanghai 200092, China. E-mail: wang_jianying@tongji.edu.cn; zfchen@tongji.edu.cn

[b]Department of Chemical and Biomolecular Engineering and Ralph O'Connor Sustainable Energy Institute, Johns Hopkins University, Baltimore, Maryland 21218, USA

[c]State Key Laboratory of Pollution Control and Resources Reuse, College of Environmental Science & Engineering, Tongji University, 1239 Siping Road, Shanghai 200092, China

HMFOR, where reaction kinetics are strongly influenced by the local electrolyte environment.[13,14] Although the hydrogen-bond network of water facilitates proton transfer, it can also form a rigid interfacial layer that hinders the diffusion of bulky organic molecules like HMF, a shielding effect that introduces a significant yet often overlooked kinetic barrier.[15] Therefore, reconciling the requirements for optimal performance at both solid-state and solid–liquid interfaces remains a fundamental challenge in catalyst design. A key design principle emerges: engineering atomic-scale solid-state interfaces that can meanwhile modulate the interfacial solvent structure across the electric double layer, thereby alleviating mass transport limitations.

Herein, we report the rational design of a single-atom nickel-decorated tungsten carbide (Ni-WC_x) catalyst that serves as a high-performance bifunctional electrocatalyst for an advanced rZAB system capable of co-producing FDCA. Distinguished from conventional bifunctional materials, the Ni-WC_x catalyst features a reaction-selective active site architecture where atomically dispersed $Ni^{\delta+}$ centers primarily catalyze the HMFOR *via* a direct $Ni^{\delta+}/Ni^{3+}$ redox cycle, while adjacent electronically modulated W sites serve as the principal centers for the ORR. This site-differentiation strategy effectively minimizes competitive adsorption between HMF and oxygen species, allowing the catalyst to achieve 99% FDCA selectivity at 1.45 V *vs.* RHE and an impressive ORR half-wave potential ($E_{1/2}$) of 0.855 V that surpasses commercial Pt/C. Through a combination of *in situ* FTIR spectroscopy, molecular dynamics (MD) simulations, and density functional theory (DFT) calculations, we elucidate a unique promotion mechanism: the $Ni^{\delta+}$ sites not only provide optimal binding for HMF adsorption but also electrostatically disrupt the rigid interfacial hydrogen-bond network of water, thereby facilitating the mass transfer of bulky organic reactants and OH^- to the catalytic surface. When deployed as the air cathode in an HMF-assisted rZAB, the catalyst enables an ultra-low charge–discharge voltage gap of 0.71 V at 20 mA cm^{-2}, a high power density of 124.7 mW cm^{-2}, and excellent long-term stability over 200 hours of continuous operation, all while maintaining uninterrupted FDCA generation. This work establishes a new catalyst design paradigm that highlights the importance of atomic-level control over both the solid-state and solid–liquid interfaces to enhance reaction kinetics and mass transport in advanced electrochemical systems.

Results and discussion

Synthesis and characterization of the Ni-WC_x

The Ni-WC_x catalyst was synthesized *via* a facile sol–gel method followed by pyrolysis. Briefly, dopamine (DA) was employed as a strong chelating agent to uniformly disperse metal atoms within a W-DA-Ni precursor, which was pyrolyzed under nitrogen to yield Ni-WC_x nanoparticles supported on carbon, as shown in Fig. 1a. Scanning electron microscopy (SEM) image shows that Ni-WC_x exhibits a hierarchical hydrangea-like morphology composed of layered nanosheets assembled into microspheres (Fig. 1b), which facilitates active site exposure and provides ample electrode/electrolyte interface. This morphology remains consistent with that of pristine WC_x (Fig. S1), indicating that Ni incorporation does not alter the overall structure. Transmission electron microscopy (TEM) images confirm that the nanoparticles are firmly embedded in the carbon matrix, as depicted in Fig. 1c and S2, and high-resolution TEM (HRTEM) reveals a lattice spacing of 0.251 nm corresponding to the (100) plane of WC (Fig. 1d).

Atomic-scale aberration-corrected high-angle annular dark-field scanning transmission electron microscopy (HAADF-STEM) image further reveals isolated Ni atoms incorporated into W-atom arrays (Fig. 1e). The intensity contrast, consistent with the atomic numbers of Ni ($Z = 28$) and W ($Z = 74$), along with line–scan profiles (Fig. 1f) and 3D atom mapping (Fig. 1g), confirms the atomic dispersion of Ni on WC_x.[16] Energy-dispersive X-ray (EDX) elemental mappings demonstrate homogeneous distribution of Ni, W and C without detectable Ni agglomeration (Fig. 1h), collectively verifying the successful synthesis of atomically dispersed Ni on WC_x.

X-ray diffraction (XRD) patterns of both Ni-WC_x and WC_x correspond to hexagonal WC (JCPDS No. 01-2755) and W_2C (JCPDS No. 03-5411) phases, with the (100) plane of WC being predominant (Fig. 2a).[17,18] The absence of Ni-related crystalline phases and the reduced overall crystallinity of Ni-WC_x is consistent with Ni single atoms incorporated into the WC_x lattice. Raman spectroscopy further supports the conclusion (Fig. S3) that the W–C vibration peaks (~675 and 802 cm^{-1}) in Ni-WC_x exhibit a red shift compared to pristine WC_x, indicating an attenuation of W–C bonds due to Ni doping.

X-ray photoelectron spectroscopy (XPS) was used to analyze the surface electronic states of Ni-WC_x (survey spectrum in Fig. S4a). The high-resolution Ni 2p spectrum (Fig. 2b) shows characteristic Ni $2p_{3/2}$ and Ni $2p_{1/2}$ peaks along with satellite features.[19–21] Deconvolution identifies contributions at 853.2 and 868.9 eV, attributed to Ni–C bonding, indicating interaction between Ni atoms and the carbon support.[22] The surface Ni content measured by XPS is 2.25 wt%, aligning closely with the bulk value of 2.33 wt% from inductively coupled plasma-optical emission spectrometry (ICP-OES).

In the W 4f spectrum of Ni-WC_x (Fig. 2c), peaks corresponding to W–C bonds are observed at 31.2 and 33.3 eV, alongside higher binding energy peaks indicative of W^{6+} species due to surface oxidation.[23,24] Notably, the W 4f peaks exhibit a positive shift compared to pristine WC_x, implying reduced electron density around W atoms due to electron transfer from the WC_x support to Ni. This electronic interaction highlights the role of Ni doping in modulating the catalyst's interfacial properties. Further support comes from the C 1s spectrum (Fig. S4b), which displays fitted peaks for C–W/Ni (283.0 eV), C–C (284.1 eV), and C–O (285.3 eV).[22]

Synchrotron-based X-ray absorption fine structure (XAFS) analysis was conducted to probe the local coordination and electronic states of W and Ni in Ni-WC_x. At the W L_3-edge, the XANES spectrum of Ni-WC_x (Fig. 2d) displays enhanced white-line intensity relative to WC_x, consistent with XPS results and indicative of an increased oxidation state of W due to Ni doping.[25] FT-EXAFS analysis reveals that Ni-WC_x maintains

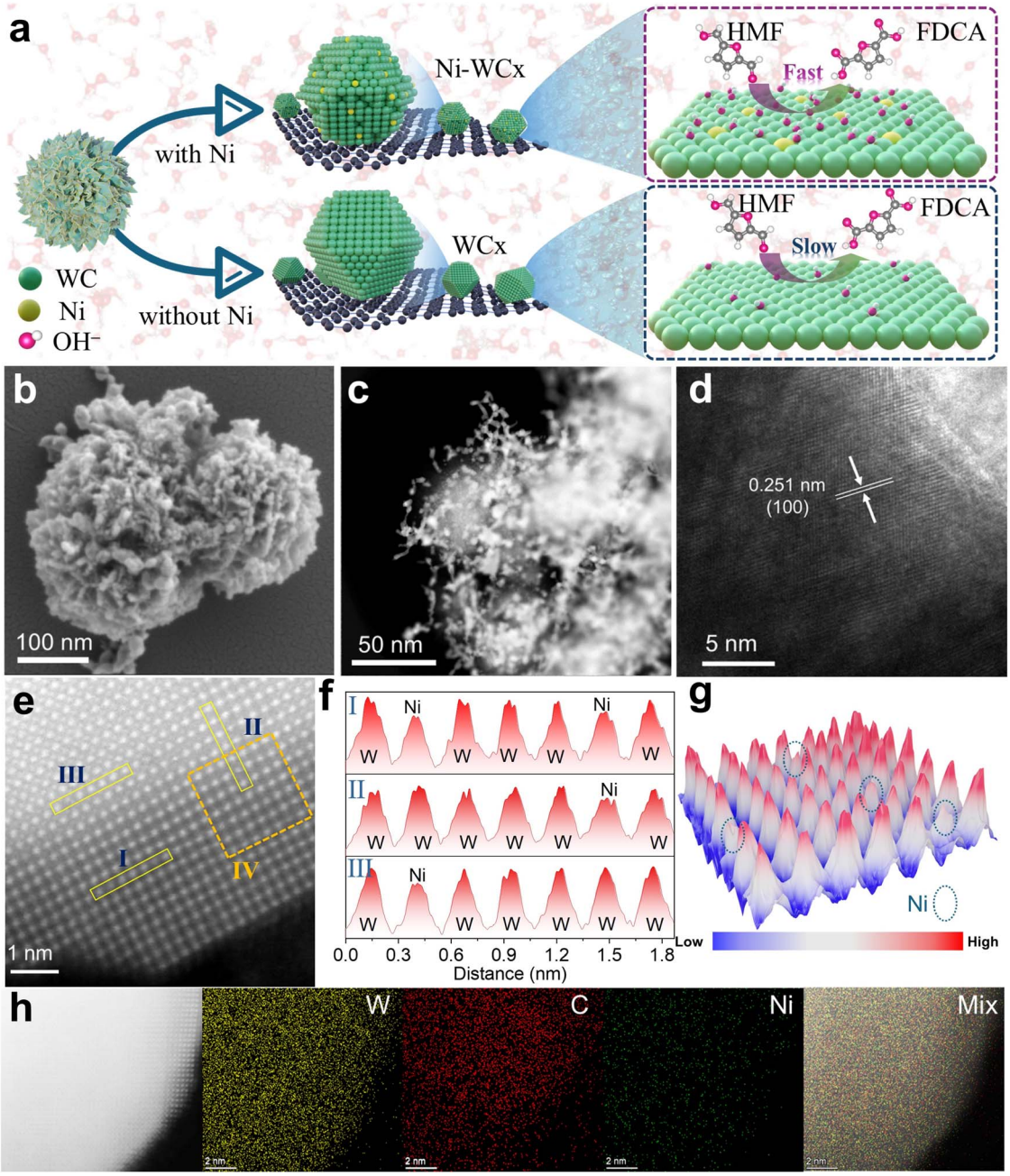

Fig. 1 Morphological and structural characterization of the synthesized materials. (a) Schematic illustration of Ni-WC_x and WC_x, highlighting the atomically engineering effect toward HMFOR. (b) SEM, (c) TEM, and (d) HRTEM images of Ni-WC_x. (e) HAADF-STEM image of Ni-WC_x, revealing atomic-scale features. (f) Corresponding intensity profile and (g) 3D atomic-resolution topographic representation derived from IV region in (e). (h) Elemental mapping of W, C and Ni in Ni-WC_x.

a primary W–C coordination shell similar to WC_x, though with slightly increased coordination numbers in both W–C and W–W/Ni paths (Fig. 2e, S5 and Table S1).

For the Ni K-edge, the XANES spectrum (Fig. 2f) confirms the presence of oxidized $Ni^{\delta+}$ species, with an average valence state of approximately +1.52 derived from linear combination fitting (Fig. S6), in agreement with charge transfer from W to Ni as inferred from XPS and W L_3-edge data.[26,27] The FT-EXAFS spectrum at the Ni K-edge (Fig. 2g) exhibits a main peak at 1.80 Å assigned to Ni–C coordination, and a distinct secondary peak at 2.84 Å corresponding to Ni–W scattering. The absence of Ni–Ni paths and the presence of Ni–W bonding provide direct evidence for atomic dispersion and substitutional doping of Ni into W sites. This conclusion is further supported by wavelet transform (WT) analysis (Fig. 2i). Quantitative EXAFS fitting (Fig. 2h, S7 and Table S1) yields a Ni–C coordination number of 3.5, comparable to the W–C coordination number (3.8) in WC_x, corroborating the substitutional doping model. Together, these

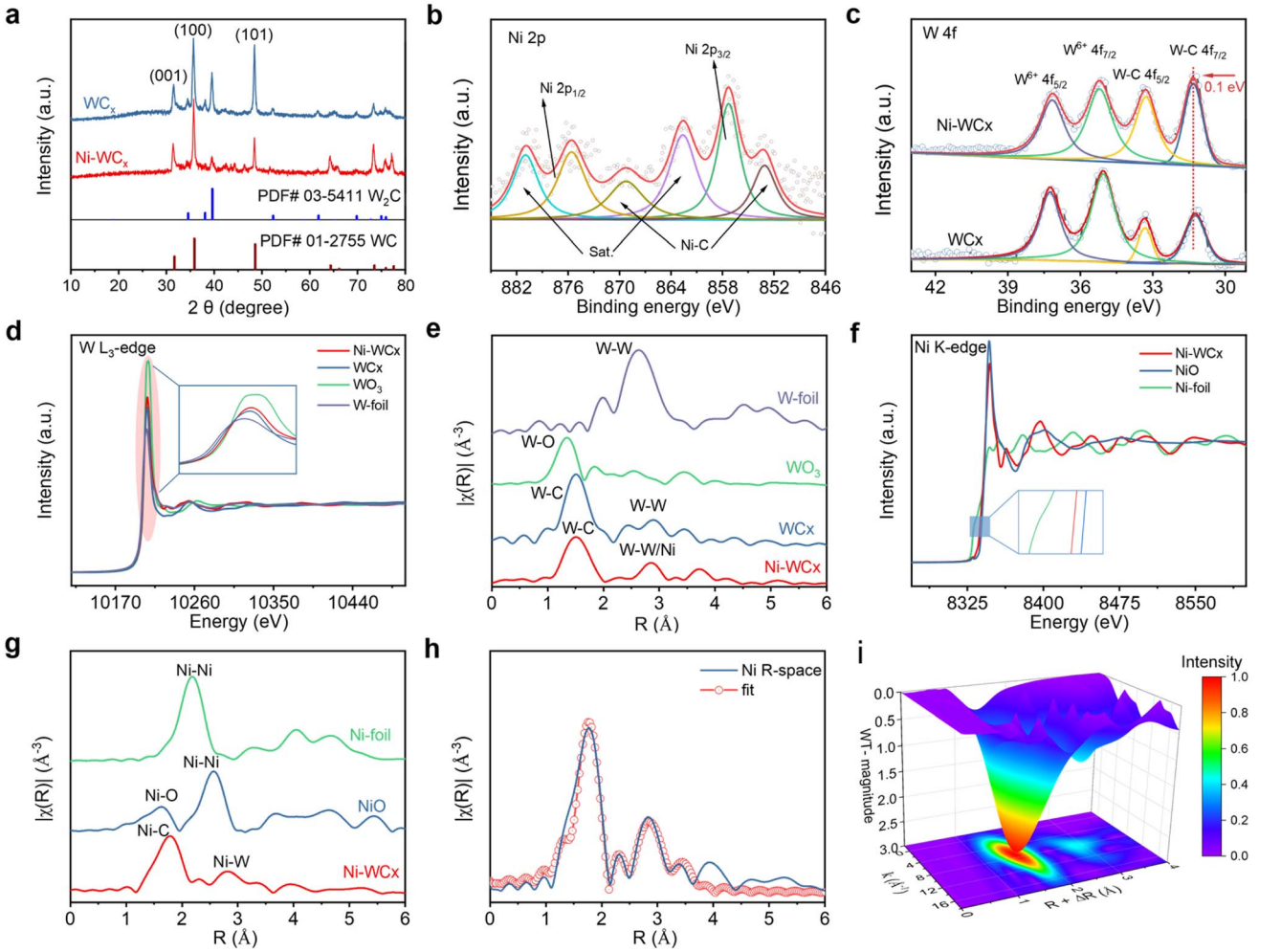

Fig. 2 Structural characterization. (a) XRD patterns of Ni-WC_x and WC_x. High-resolution XPS spectra of (b) Ni 2p for Ni-WC_x and (c) W 4f for both Ni-WC_x and WC_x. (d) Normalized XANES, and (e) FT-EXAFS spectra at the W L_3-edge. (f) Normalized XANES and (g) FT-EXAFS spectra at the Ni K-edge. (h) Corresponding fitting curves for the FT-EXAFS spectrum at the Ni K-edge for Ni-WC_x, presented in R space. (i) Wavelet transform analysis of the EXAFS spectrum at the Ni K-edge for Ni-WC_x.

results unequivocally confirm the successful incorporation of atomically dispersed $Ni^{\delta+}$ into the WC_x framework.

Performance of electrocatalytic oxidation of HMF

The electrocatalytic HMFOR performance of Ni-WC_x was assessed in a three-electrode system with 1.0 M KOH. As shown by the linear sweep voltammetry (LSV) curves in Fig. 3a, without HMF, the catalyst exhibits only a minor pre-wave at 1.36 V *vs.* RHE prior to the onset of OER, which is associated with oxidation of Ni species.[28] Upon adding 20 mM HMF, a substantial current increase occurs following Ni oxidation. The potential required to reach 10 mA cm^{-2} is significantly lower for HMFOR (1.39 V) than for OER (1.56 V). The Tafel slope for HMFOR (35.7 mV dec^{-1}) is also much smaller than that for OER (57.4 mV dec^{-1}) (Fig. 3b), and the enhanced kinetics of HMFOR are further supported by electrochemical impedance spectroscopy (EIS) (Fig. S8). In stark contrast, both the WC_x and the commercial IrO_2 benchmark exhibit negligible current responses above OER background in the HMF-containing electrolyte (Fig. 3c and S9). By normalizing to the electrochemically active surface area (ECSA), Ni-WC_x maintained the highest current density compared to the counterparts, confirming the superior intrinsic activity of Ni-WC_x (Fig. S10 and S11). This result underscores the essential role of the atomically dispersed $Ni^{\delta+}$ sites toward HMFOR. Based on the linear current-concentration relationship (Fig. S12), 20 mM HMF was selected for all further tests to balance reactivity and selectivity.

Potentiostatic electrolysis at 1.45 V *vs.* RHE was used to evaluate product selectivity and Faradaic efficiency (FE) (Fig. S13–S15). High-performance liquid chromatography (HPLC) analysis (Fig. 3d and e) shows continuous consumption of HMF and accumulation of FDCA, accompanied by a visible color change from yellow to colorless. Ni-WC_x achieves 99.20% HMF conversion, 98.98% FDCA selectivity, and a FE of 97.37% (Fig. S16). The oxidation of HMF to FDCA follows two possible pathways (Fig. 3f): Pathway I begins with oxidation of the aldehyde group to form 5-hydroxymethyl-2-furancarboxylic acid (HMFCA), while Pathway II starts with hydroxyl group oxidation

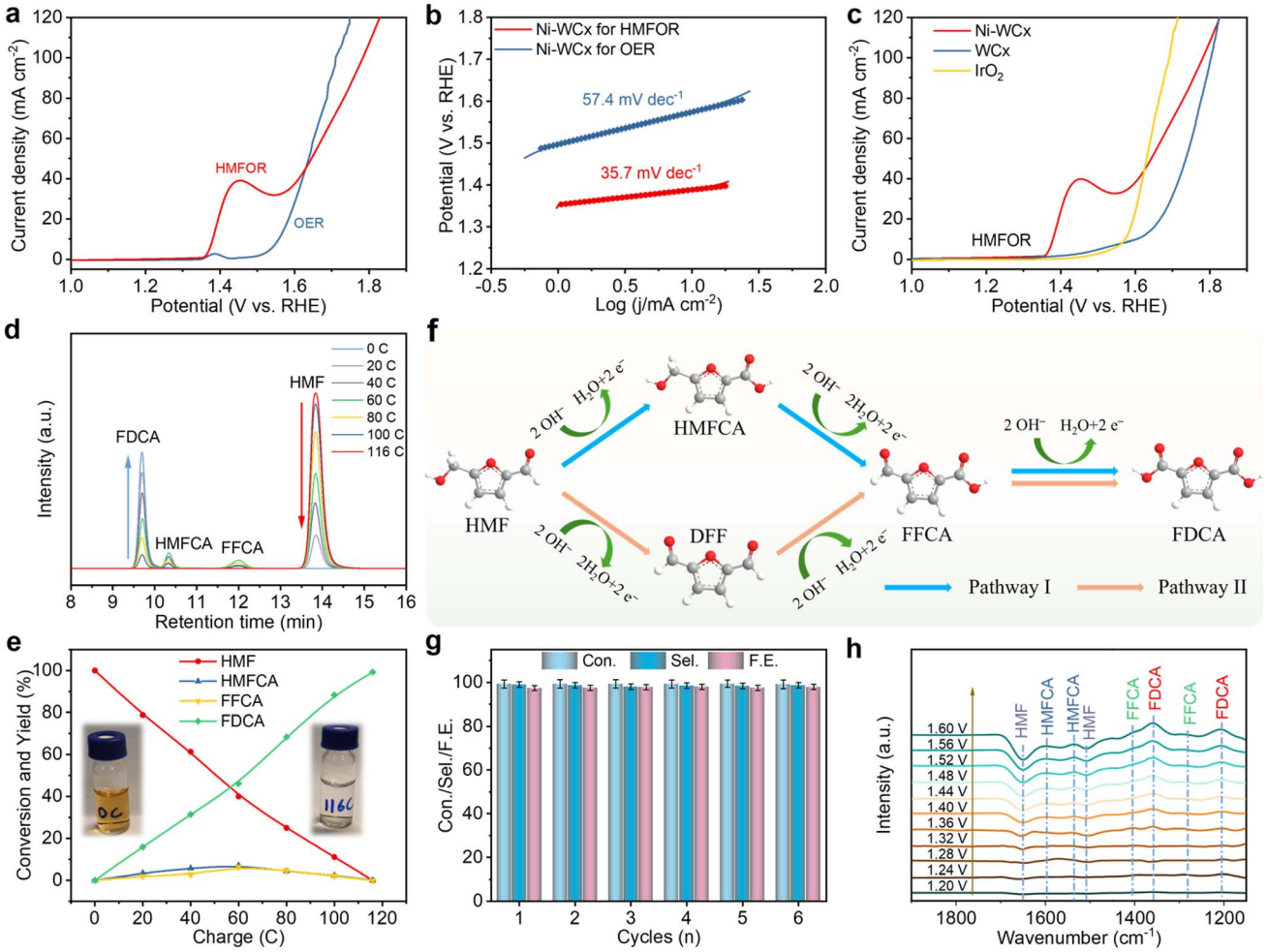

Fig. 3 Electrocatalytic HMFOR performance evaluations. (a) LSV curves of Ni-WC_x in 1 M KOH with and without 20 mM HMF, and (b) corresponding Tafel plots. (c) LSV curves illustrating the HMFOR performance of Ni-WC_x, WC_x and IrO_2. (d) HPLC curves with increasing charge accumulation at 1.45 V *vs.* RHE. (e) Charge-dependent concentration for HMF, FDCA, HMFCA, and FFCA. (f) Two principal reaction pathways for oxidation of HMF to FDCA. (g) Conversion, selectivity and Faradaic efficiency for FDCA production over six sequential electrolysis cycles. (h) *In situ* FTIR spectra of Ni-WC_x obtained at various applied potentials during HMFOR.

to yield 2,5-diformylfuran (DFF).[29] Both routes converge *via* formyl-2-furancarboxylic acid (FFCA) before final oxidation to FDCA. HPLC analysis during electrolysis detected HMFCA and FFCA, but nearly no DFF, indicating that HMFOR over the Ni-WC_x catalyst occurs predominantly through Pathway I: HMF → HMFCA → FFCA → FDCA. Recycling tests demonstrate excellent stability over six cycles with no significant activity loss (Fig. 3g and S17). Post-test characterization (TEM, XRD, XPS; Fig. S18–S20) results confirm no observable changes in morphology, structure, or chemical state, affirming the robust stability of Ni-WC_x.

To further elucidate the reaction mechanism, *in situ* Fourier transform infrared (FTIR) spectroscopy was used to track real-time species evolution during HMFOR.[30] The results showed new characteristic peaks emerging at 1.36 V *vs.* RHE (Fig. 3h), consistent with the EIS results. With increasing potential (1.40–1.60 V), product-related peaks intensify, while HMF peaks (1655 and 1519 cm^{-1}) continuously decreased. Peaks corresponding to HMFCA (1596, 1525 cm^{-1}), FFCA (1407, 1276 cm^{-1}), and FDCA (1353, 1214 cm^{-1}) were clearly observed, whereas no DFF intermediate was detected.[31,32] These results confirm further that HMFOR follows Pathway I (HMF → HMFCA → FFCA → FDCA). A slight HMF consumption observed below 1.32 V may be attributed to a minor side reaction such as the Cannizzaro reaction prior to electro-oxidation.[33]

Multi-potential step chronoamperometry was employed to identify the active species as shown in Fig. S21. In the absence of HMF, a reduction peak appears at 1.1 V, corresponding to the reduction of electrogenerated Ni^{3+} species. This peak disappears entirely when HMF is present, indicating that Ni^{3+} is chemically consumed by HMF rather than electrochemically reduced.[34] This result provides strong evidence that the $Ni^{\delta+}$/Ni^{3+} redox couple acts as the catalytic center for HMF oxidation.

The introduction of $Ni^{\delta+}$ sites is proposed to serve not only as intrinsic active centers but also to modulate the catalyst–electrolyte interface by restructuring interfacial water, thereby influencing the adsorption and transfer of OH^- and organic substrates during HMFOR.[35] To validate this, systematic

interfacial studies were conducted. Zeta potential measurements in 1.0 M KOH showed that Ni-WC_x (–25.4 mV) possesses a more negative surface charge than WC_x (–17.8 mV), signifying more OH^- in the inner Helmholtz plane (Fig. 4a).[13] This OH^--enriched interface is a direct consequence of the $Ni^{\delta+}$ sites perturbing the local solvent environment and reorganizing the hydrogen bond network.[36] Cyclic voltammetry (CV) curves between 0.7 – 1.0 V (Fig. 4b and S22) showed a pronounced *OH adsorption peak at lower potential on Ni-WC_x than on WC_x.[37] This peak decreased upon the introduction of HMF, whereas the corresponding signal on WC_x remained almost unchanged. Notably, the peak current of Ni-WC_x remained significantly higher than that of WC_x, both with and without HMF, indicating a strong co-adsorption affinity for both OH^- and HMF, a crucial feature for efficient HMFOR.[38]

To directly probe the reorganization of the hydrogen-bond network, potential-dependent *in situ* FTIR spectroscopy was applied to the O–H stretching region (ν(O–H)). For the Ni-WC_x electrode (Fig. 4c), a clear potential-dependent blueshift occurred in the ν(O–H) bands, particularly for those of non-hydrogen-bonded water molecules, indicating a weakened interfacial hydrogen-bond network due to electrostatic effects from accumulated OH^- near $Ni^{\delta+}$ sites.[39] In contrast, the ν(O–H) band for WC_x remained stable across potentials (Fig. 4d), suggesting a rigid hydrogen-bond network that impedes OH^- adsorption and transport. These results demonstrate that $Ni^{\delta+}$ incorporation fundamentally alters interfacial water dynamics, forming an electrostatically modulated environment that enhances mass transfer and promotes HMFOR kinetics.

To elucidate how $Ni^{\delta+}$ sites reorganize interfacial water at the molecular level, molecular dynamics (MD) simulations were carried out. MD snapshots and concentration profiles of oxygen atoms in water normal to the surface (Fig. 4e–g) show that $Ni^{\delta+}$ strengthens electrostatic catalyst–water interactions, drawing water closer to the surface.[35] Analysis of the hydrogen-bond (H-bond) network *versus* distance from the surface (Fig. 4h) reveals that Ni-WC_x has fewer H-bonds and a longer average bond length (3.042 Å) in the first water layer (~3 Å) compared to WC_x

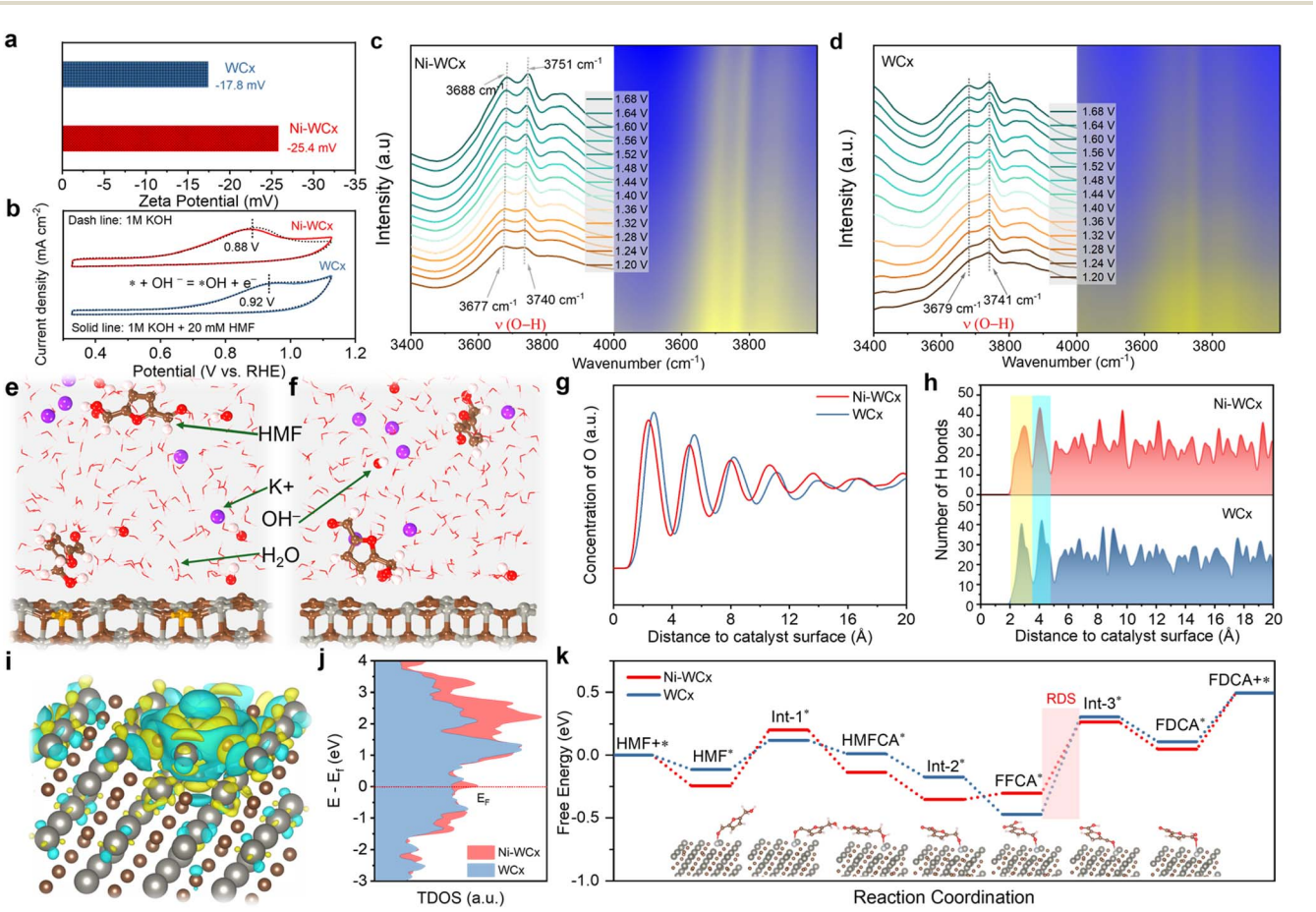

Fig. 4 Mechanism investigation of catalyst–electrolyte interface in HMFOR. (a) Zeta potential of Ni-WC_x and WC_x in 1 M KOH. (b) CV curves of Ni-WC_x and WC_x in KOH with and without 20 mM HMF. *In situ* FTIR spectra highlighting the non-hydrogen bonded O–H stretching vibration mode acquired within 1.20–1.60 V for (c) Ni-WC_x and (d) WC_x in 1 M KOH, accompanied by corresponding 2D visualizations. MD simulated representative snapshots of electrode–electrolyte interface for (e) Ni-WC_x and (f) WC_x, with Ni, W and C atoms represented by yellow, gray and brown spheres, respectively. (g) Spatially resolved concentration profiles of oxygen atoms in water, plotted as a function of distance normal to the Ni-WC_x and WC_x surfaces. (h) Statistical distributions of hydrogen bond counts as a function of distance normal to the Ni-WC_x and WC_x surfaces. (i) Differential charge density map of Ni-WC_x, indicating regions of charge accumulation (yellow) and depletion (blue). (j) TDOS for Ni-WC_x and WC_x. (k) Free energy diagrams for the HMFOR pathway on Ni-WC_x and WC_x.

(3.032 Å), whereas the second layer (~4.5 Å) shows higher H-bond density. Further analysis of the MD trajectories reveals that the lateral diffusion coefficient of interfacial HMF, extracted from the mean-squared displacement parallel to the surface (Fig. S23), is significantly larger on Ni-WC_x than on WC_x. Additionally, angular distribution analysis (Fig. S24) shows that HMF on Ni-WC_x adopts a preferred "lying-down" orientation, which brings the reactive aldehyde group into close proximity with the active sites and facilitates surface interaction, whereas it exhibits a random orientation on WC_x. These results indicate that $Ni^{\delta+}$ induces a targeted reconstruction of the interfacial H-bond network, rather than inducing a broad destabilization.[40] The disrupted first layer forms a dynamic, loose microenvironment that reduces mass transfer resistance for bulky HMF molecules and facilitates OH^- shuttling.

To elucidate the origin of the enhanced HMFOR activity, systematic DFT calculations were conducted. Charge density difference plots (Fig. 4i) reveal significant interfacial charge redistribution in Ni-WC_x, with electron accumulation between Ni and the WC_x support, confirming strong electronic coupling. Correspondingly, the total density of states (TDOS) near the Fermi level is higher in Ni-WC_x than in WC_x (Fig. 4j), indicating improved charge transfer. Projected density of states (PDOS) analysis (Fig. S25) further shows that $Ni^{\delta+}$ induces delocalization of electrons in adjacent W 5d orbitals.[41] This electronic modulation reshapes the surface electrostatic environment, strengthening interactions with interfacial water and providing a fundamental rationale for the restructured hydrogen-bond network observed in MD and FTIR. The optimized electronic structure of Ni-WC_x leads to superior reaction kinetics. HMF adsorbs more strongly on the Ni site (–0.246 eV) than on WC_x (–0.112 eV), with the aldehyde group tilting toward Ni in an ideal configuration for C–H activation (Fig. S26).[42] Free energy calculations along Pathway I (Fig. 4k and S27) identify FFCA* dehydrogenation as the rate-determining step (RDS). Ni doping drastically reduces this barrier from 0.776 eV (WC_x) to 0.569 eV (Ni-WC_x). These results demonstrate that synergistic electronic coupling between $Ni^{\delta+}$ and WC_x enhances intermediate adsorption and reduces the RDS energy barrier, thereby significantly improving intrinsic HMFOR activity.

Performance of oxygen reduction reaction

The ORR performance of Ni-WC_x was systematically assessed in O_2-saturated 0.1 M KOH using the rotating disk electrode (RDE) method, with WC_x and commercial Pt/C as benchmarks. Preliminary CV curves confirm intrinsic ORR activity for both Ni-WC_x and WC_x (Fig. S28). LSV curves in Fig. 5a show that Ni-WC_x exhibits a higher half-wave potential ($E_{1/2}$ = 0.855 V) and larger limiting current density (J_L = 6.16 mA cm^{-2}) than both WC_x ($E_{1/2}$ = 0.747 V, J_L = 4.98 mA cm^{-2}) and Pt/C ($E_{1/2}$ = 0.850 V, J_L = 5.89 mA cm^{-2}). The Tafel slope of Ni-WC_x (39.1 mV dec^{-1}) is also significantly lower than those of WC_x (64.9 mV dec^{-1}) and Pt/C (63.6 mV dec^{-1}), indicating faster reaction kinetics, as illustrate in Fig. 5b. This superior catalytic activity is further supported by its superior kinetic current sdensity (J_k, Fig. 5c) and ECSA-normalized current density (Fig. S29). To elucidate the ORR pathway, the number of electrons transferred (n) was determined *via* rotating ring-disk electrode (RRDE) measurements and Koutecky–Levich (K–L) analysis. RRDE results (Fig. 5d) show an n value of 3.9 and a low H_2O_2 yield (<8%), consistent with the $4e^-$ pathway. K–L plots from LSVs at multiple rotation speeds also confirm $n \approx 4.0$ (Fig. S30), reinforcing the dominant $4e^-$ reduction mechanism.

The long-term durability of Ni-WC_x was assessed *via* chronoamperometry measurement. As can be seen in Fig. 5e, Ni-WC_x retained 88.1% of its initial current after 20 hours, significantly outperforming Pt/C (75.2%). Post-test ORR polarization curves (Fig. S31) show that the change of $E_{1/2}$, onset potential and J_L of Ni-WC_x was insignificant, indicating little loss of intrinsic activity. TEM image (Fig. S32) reveals that the hydrangea-like microspheres and nanosheet subunits were preserved without noticeable aggregation or collapse. XRD pattern after ORR (Fig. S33) retained the characteristic WC/W_2C reflections without phase change, while XPS analysis (Ni 2p and W 4f; Fig. S34) confirms that Ni remained in an oxidized $Ni^{\delta+}$ state and the W–C framework was largely maintained. These results collectively demonstrate the robust chemical and structural stability of Ni-WC_x under harsh oxidative conditions.

The bifunctional performance was quantified using the potential gap ΔE, defined as $\Delta E = E_{j=10}$ (OER/HMFOR) – $E_{1/2}$ (ORR).[43] A smaller ΔE indicates better catalytic reversibility. Ni-WC_x achieves an exceptionally low ΔE of 0.54 V for the ORR||HMFOR couple, considerably lower than 0.72 V for ORR||OER on the same catalyst (Fig. 5f). This result underscores the kinetic advantage of replacing OER with HMFOR. Moreover, this performance surpasses most recently reported non-noble metal catalysts (Table S2).

To definitively ascertain the active site identity for ORR, selective site-blocking investigations were conducted utilizing thiocyanate (SCN^-), a strong blocking agent for Ni sites. As shown in Fig. S35, the cathodic current observed on the Ni-WC_x electrode remained largely unperturbed following the introduction of 10 mM KSCN into the O_2-saturated 0.1 M KOH electrolyte, indicating a substantial resistance to selective poisoning. Specifically, this limited effect suggests that $Ni^{\delta+}$ sites are not the primary active centers for the ORR, or at least that their blockage does not suppress the main reaction pathway.

To elucidate the ORR mechanism on Ni-WC_x at the atomic level, DFT calculations were performed to evaluate the thermodynamics of key intermediates (*OOH, *O, *OH) on different active sites of W and Ni sites on Ni-WC_x, as well as W site on pristine WC_x (Fig. 5g and S36).[44] The free energy diagrams at U = 0 V show a downhill trend for all sites (Fig. 5h). At the equilibrium potential (U = 1.23 V), the RDS on the Ni site is *OOH dissociation to *O, with a high energy barrier of 1.13 eV. In contrast, the RDS on W sites (both in Ni-WC_x and WC_x) is *OH desorption. Notably, the energy barrier for this step is significantly lower on the W site of Ni-WC_x (0.64 eV) than on pristine WC_x (0.86 eV), identifying W atoms near Ni as the primary ORR active sites and highlighting the promotional role of Ni doping.

To understand the electronic origin of the reduced barrier, the Crystal Orbital Hamilton Population (COHP) analysis was

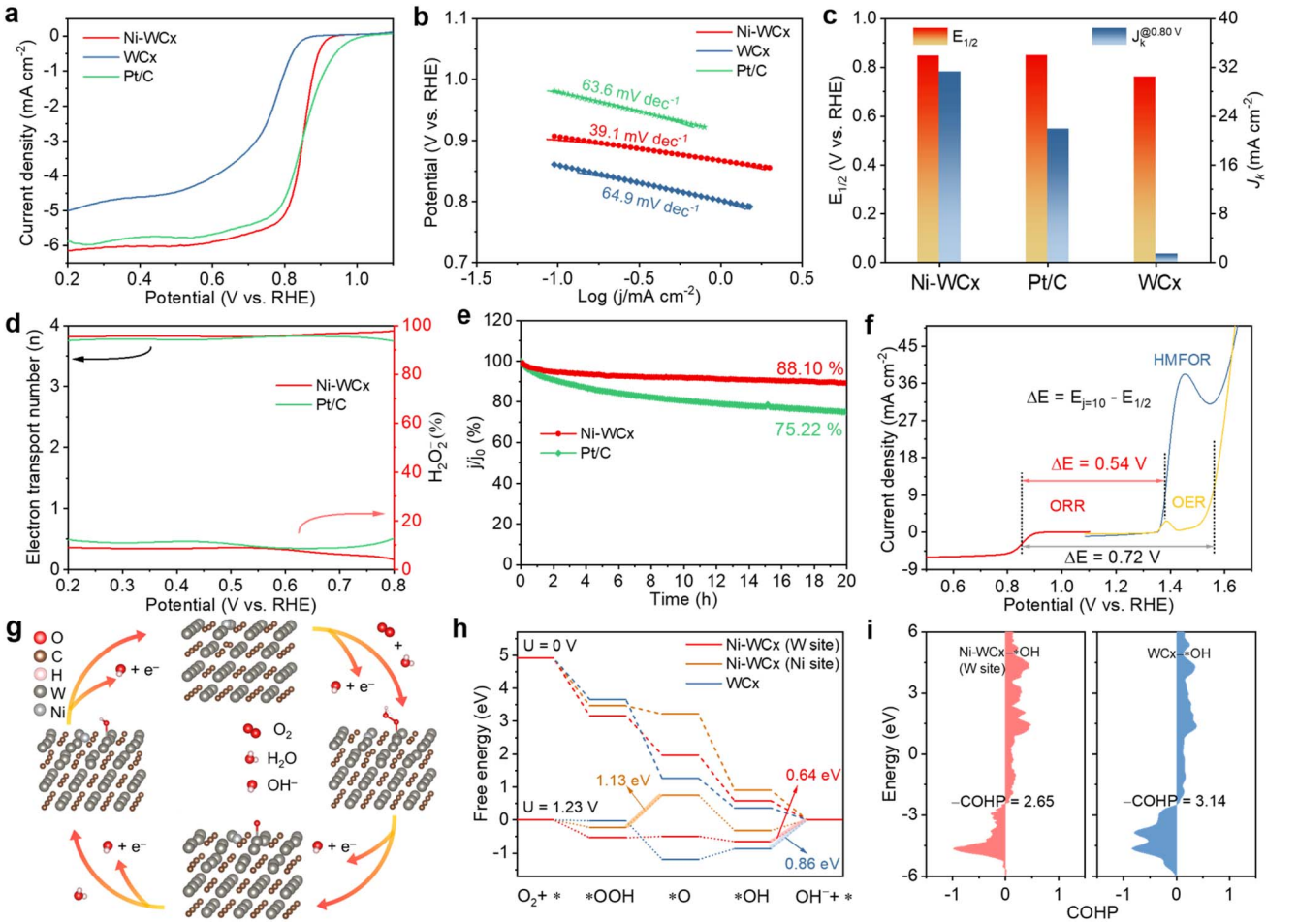

Fig. 5 Electrocatalytic ORR performance. (a) ORR polarization curves in O_2-saturated 0.1 M KOH at a rotating rate of 1600 rpm, (b) Tafel plots, and (c) analysis of $E_{1/2}$ and J_k at 0.80 V of Ni-WC_x, WC_x and Pt/C. (d) Determination of electron transfer numbers and H_2O_2 yield during the ORR process. (e) Chronoamperometry stability assessment conducted at 0.40 V *vs.* RHE. (f) Overall polarization curves of Ni-WC_x toward the ORR and OER/HMFOR. (g) Proposed mechanism elucidating ORR on Ni-WC_x. (h) Free energy diagram of ORR on Ni-WC_x and WC_x. (i) COHP analysis and the corresponding ICOHP values quantifying the bonding interaction between adsorbed *OH and Ni-WC_x and WC_x surfaces.

conducted to probe the bonding strength of the key *OH intermediate.[45] The integrated COHP (ICOHP) value for the W–OH bond on Ni-WC_x is $|-2.65|$, smaller than that on WC_x ($|-3.14|$), indicating a weaker W–OH interaction that facilitates *OH removal (Fig. 5i and S37). These results confirm that Ni doping electronically modulates adjacent W sites, optimizing the adsorption/desorption of oxygen intermediates and enhancing intrinsic ORR activity, consistent with experimental observations.

It is noteworthy that Ni-WC_x catalyst exhibits reaction-selective active sites, a critical design feature that enables its exceptional bifunctional performance. Different from conventional bifunctional catalysts where the same active site mediates both reactions, Ni-WC_x leverages a synergistic dual-site mechanism: atomically dispersed $Ni^{\delta+}$ centers catalyze HMFOR through direct participation in the $Ni^{\delta+}/Ni^{3+}$ redox cycle, while adjacent W sites, electronically modulated by Ni incorporation, serve as the primary ORR active centers with optimized oxygen intermediate binding. This site-differentiation strategy not only maximizes the intrinsic activities of both reactions but also minimizes potential competitive adsorption between HMF and O_2-derived species, contributing to the superior performance in HMF-assisted Zn–air batteries.

Performance of HMF-assisted rechargeable Zn–air redox battery

Utilizing the outstanding bifunctional activity of Ni-WC_x, an HMF-assisted rechargeable rZAB was constructed to assess its practical performance (Fig. 6a). Substituting the OER with HMFOR offers multiple key benefits: it enables the coproduction of valuable chemicals, lowers the charging voltage to mitigate cathode degradation from high overpotentials,[46,47] and eliminates O_2 bubble formation, thereby enhancing interfacial stability, particularly at high current densities.[48,49]

For comparison, conventional rZABs with Ni-WC_x or Pt/C–IrO_2 as a cathode for ORR/OER were also assembled. The HMF-assisted battery achieved an open-circuit voltage (OCV) of 1.483 V, comparable to the ORR/OER Ni-WC_x battery (1.485 V) and higher than the ORR/OER Pt/C–IrO_2 battery (1.457 V, Fig. 6b

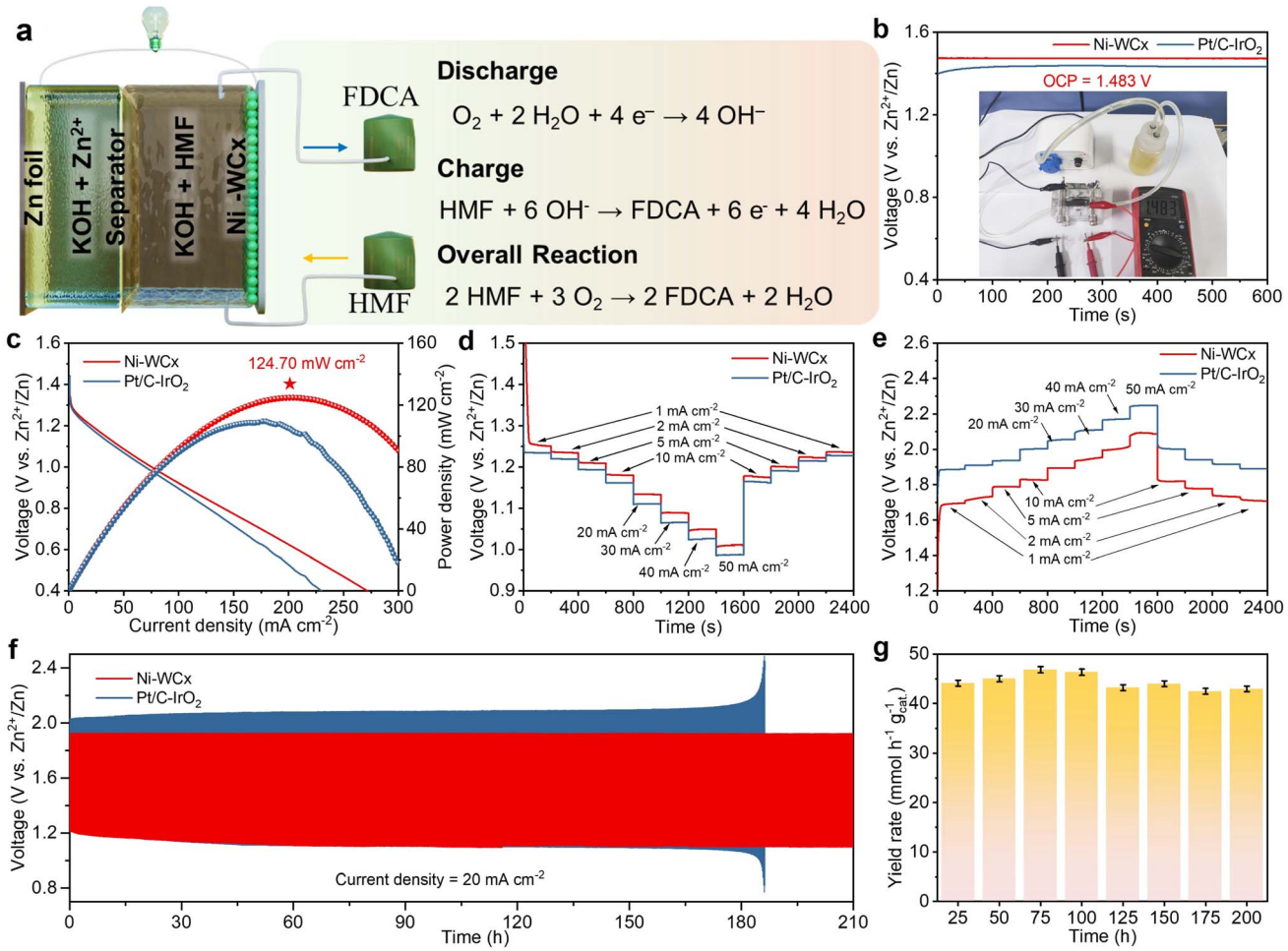

Fig. 6 Rechargeable Zn–air battery performances evaluations. (a) Schematic illustration of HMF-assisted flow-type rZAB. (b) Open-circuit voltages. (c) Discharge polarization curves and corresponding power density profiles for the rZAB. (d) Galvanostatic discharge and (e) galvanostatic charge curves under different current densities. (f) Long-term cycling stability assessed *via* galvanostatic discharge–charge measurements at a current density of 20 mA cm^{-2}, and (g) the associated yield rate of FDCA.

and S38). Charge–discharge polarization curves showed that the HMF-assisted system maintains a smaller voltage gap than that using a Pt/C–IrO_2 cathode across current densities from 1 to 75 mA cm^{-2} (Fig. S39), indicating improved energy efficiency. The gap increases at higher currents due to competing OER.

The HMF-assisted rZAB reached a peak power density of 124.7 mW cm^{-2} (Fig. 6c), on par with the ORR/OER Ni-WC_x battery and superior to the ORR/OER Pt/C–IrO_2 battery (Fig. S40), confirming that HMF addition does not hinder discharge performance. It delivered a high specific capacity of 749.85 mAh g^{-1} at 20 mA cm^{-2}, exceeding the ORR/OER Pt/C–IrO_2 battery (720.02 mAh g^{-1}, Fig. S41). The HMF-assisted rZAB also exhibited excellent rate capability with stable discharge plateaus from 1 to 50 mA cm^{-2} and rapid potential recovery after high-current pulses (Fig. 6d). Constant-current charging confirmed consistently lower charging voltages for the HMF-assisted system across all currents (Fig. 6e and S42), demonstrating that HMFOR effectively reduces charging overpotential and improves energy efficiency.

To evaluate the viability of the HMF-assisted battery as a dual-output system, its long-term cycling performance was tested at 20 mA cm^{-2}. The HMF-assisted rZAB exhibited a significantly smaller initial voltage gap (charge: 1.925 V, discharge: 1.214 V) than the ORR/OER Pt/C–IrO_2 battery (2.031 V, 1.234 V), achieving a high initial round-trip efficiency of 63.1% (Fig. 6f). After 200 hours of cycling, it maintained excellent stability with minimal voltage decay and a round-trip efficiency of 56.4%. In contrast, the ORR/OER Pt/C–IrO_2 battery showed severe polarization and failed after ~180 hours, highlighting the superior durability and energy efficiency of the HMF-assisted system.

Simultaneously, the battery continuously produced FDCA at a high rate exceeding 42.50 mmol h^{-1} $g_{cat}{}^{-1}$ throughout the 200-hours test (Fig. 6g). This dual functionality, which combining stable energy storage with efficient chemical production, outperforms most previously reported hybrid rZAB systems (Table S3). Furthermore, a single HMF-assisted rZAB successfully powered an electronic timer for over 24 hours (Fig. S43), demonstrating practical applicability. These results

thus establish the HMF-assisted rZAB as a highly efficient and durable bifunctional system that integrates energy storage with sustainable chemical synthesis.

Conclusions

In summary, we have successfully developed a single-atom Ni-decorated tungsten carbide catalyst with exceptional bifunctional activity for both HMF oxidation and oxygen reduction. When deployed in a hybrid zinc–air battery, this catalyst enables a system that simultaneously achieves a low charge–discharge voltage gap, outstanding cycling stability, and continuous production of FDCA with high selectivity and Faradaic efficiency.

Beyond its catalytic performance, this work reveals a synergistic mechanism that transcends conventional active-site design. We demonstrate that atomically dispersed $Ni^{\delta+}$ sites serve not only as intrinsic active centers but also as atomic-level modulators of the catalyst–electrolyte interface. Through integrated experiments and multiscale simulations, we show that $Ni^{\delta+}$ incorporation reconstructs the interfacial water structure, disrupting rigid hydrogen-bond networks and alleviating mass transport limitations for bulky organic molecules. By highlighting the critical role of interfacial solvent engineering alongside electronic structure optimization, this study establishes a new design paradigm for multifunctional electrocatalysts, opening avenues for integrated energy conversion and sustainable chemical synthesis.

Author contributions

Xiaoyang He: conceptualization, data curation, formal analysis, investigation, methodology, software, writing – original draft, and writing – review & editing; Dengke Xiong, Kaiyan Zhang, Wei Wang, Shujie Xue: methodology, data curation, formal analysis, investigation, and software; Jianying Wang, Deli Wu: conceptualization, resources, supervision; Zuofeng Chen: conceptualization, formal analysis, investigation, methodology, resources, funding acquisition, supervision, project administration, and writing – review & editing.

Conflicts of interest

There are no conflicts of interest to declare.

Data availability

The data supporting this article have been included as part of the supplementary information (SI). Supplementary information: details of Experimental section including chemical and materials; material characterizations; product separation and analysis; *in situ* FTIR; DFT calculation and MD methods; additional morphological; structural and compositional characterizations of Ni-WC_x and contrast samples; stability characterizations; standard curves of product analysis, calculated Faradaic efficiencies; SI Figures and Tables and optical photograph of the HMF-assisted Zn–air battery. See DOI: https://doi.org/10.1039/d5sc09133k.

Acknowledgements

This work was supported by the National Key R&D Program of China (2024YFA1211004), the National Natural Science Foundation of China (22402150), the Natural Science Foundation of Shanghai Municipality (23ZR1464800, 24ZR1470200), the Fundamental Research Funds for the Central Universities (22120240296).

References

1 G. Li, R. Wang, J. Pang, A. Wang, N. Li and T. Zhang, *Chem. Rev.*, 2024, **124**, 2889–2954.
2 X. Liu, X. He, D. Xiong, G. Wang, Z. Tu, D. Wu, J. Wang, J. Gu and Z. Chen, *ACS Catal.*, 2024, **14**, 5366–5376.
3 L. Guo, X. Zhang, L. Gan, L. Pan, C. Shi, Z. F. Huang, X. Zhang and J. J. Zou, *Adv. Sci.*, 2023, **10**, 2205540.
4 D. Chen, Y. Ding, X. Cao, L. Wang, H. Lee, G. Lin, W. Li, G. Ding and L. Sun, *Angew. Chem., Int. Ed.*, 2023, **62**, e202309478.
5 Z. Li, L. Sun, Y. Zhang, Y. Han, W. Zhuang, L. Tian and W. Tan, *Coord. Chem. Rev.*, 2024, **510**, 215837.
6 M. Wu, Y. Xu, J. Luo, S. Yang, G. Zhang, L. Du, H. Luo, X. Cui, Y. Yang and S. Sun, *Angew. Chem., Int. Ed.*, 2024, **136**, e202410845.
7 Y. Wang, S. Lu, M. Yang, Z. Zhang and J. Zhang, *Mater. Today Sustain.*, 2024, **25**, 100630.
8 Y. Lin, B. Chen, D. Huang, Z. Yang, A. Lu, Z. Shi, Y. Liu, J. Fang, H. Li and T. Zhai, *Angew. Chem., Int. Ed.*, 2025, **137**, e202502151.
9 R. Zhao, Q. Wang, Y. Yao, R. Wang, L. Zhao, Z. Hu, C.-W. Kao, T.-S. Chan, W. Li, Q. Zheng, J. Wang, X. Zou, K. Wang, J. Dai, X.-K. Gu and L. Zhang, *Sci. Adv.*, 2025, **11**, eadu1602.
10 Y. Li, Y. Li, H. Sun, L. Gao, X. Jin, Y. Li, Z. Lv, L. Xu, W. Liu and X. Sun, *Nano-Micro Lett.*, 2024, **16**, 139.
11 Z. Li, W. Na, C. Tian, J. Dong, L. Tian, M. Ma, T. Li and Y. Zhang, *Chem. Eng. J.*, 2025, **526**, 171146.
12 Y. Liu, T. G. Kelly, J. G. Chen and W. E. Mustain, *ACS Catal.*, 2013, **3**, 1184–1194.
13 P. Zhou, X. Lv, S. Tao, J. Wu, H. Wang, X. Wei, T. Wang, B. Zhou, Y. Lu, T. Frauenheim, X. Fu, S. Wang and Y. Zou, *Adv. Mater.*, 2022, **34**, 2204089.
14 D. Xiao, X. Bao, D. Dai, Y. Gao, S. Si, Z. Wang, Y. Liu, P. Wang, Z. Zheng, H. Cheng, Y. Dai and B. Huang, *Adv. Mater.*, 2023, **35**, 2304133.
15 Z. Yang, L. Chen, Y. Yin, C. Wei, Z. Xue and T. Mu, *Energy Environ. Sci.*, 2024, **17**, 8801–8809.
16 S. Li, B. Chen, Y. Wang, M.-Y. Ye, P. A. van Aken, C. Cheng and A. Thomas, *Nat. Mater.*, 2021, **20**, 1240–1247.
17 L. Wang, Z. Xu, C.-H. Kuo, J. Peng, F. Hu, L. Li, H.-Y. Chen, J. Wang and S. Peng, *Angew. Chem., Int. Ed.*, 2023, **135**, e202311937.

18 H. Li, W. Wang, S. Xue, J. He, C. Liu, G. Gao, S. Di, S. Wang, J. Wang, Z. Yu and L. Li, *J. Am. Chem. Soc.*, 2024, **146**, 9124–9133.
19 D. Xiong, X. He, Z. Zhu, T. Liu, D. Wu, Y. Zou and Z. Chen, *Adv. Funct. Mater.*, 2025, e18434, DOI: 10.1002/adfm.202518434.
20 Z. Tu, X. He, X. Liu, D. Xiong, J. Zuo, D. Wu, J. Wang and Z. Chen, *Chinese J. Catal.*, 2024, **58**, 146–156.
21 H. Yang, J. Dong, X. Gao, C. Ni, Z. Li, Y. Liu, J. Li, X. He, W. Tan, L. Feng and L. Tian, *Small*, 2025, **21**, 2410399.
22 B. C. Bayer, D. A. Bosworth, F. B. Michaelis, R. Blume, G. Habler, R. Abart, R. S. Weatherup, P. R. Kidambi, J. J. Baumberg, A. Knop-Gericke, R. Schloegl, C. Baehtz, Z. H. Barber, J. C. Meyer and S. Hofmann, *J. Phys. Chem. C*, 2016, **120**, 22571–22584.
23 X. Chen, C. Chen, M. M. Amjad, D. Sun, B. Sun and K. Zhang, *Appl. Catal. B-Environ.*, 2024, **344**, 123644.
24 C. Griesser, S. Diaz-Coello, M. Olgiati, W. F. do Valle, T. Moser, A. Auer, E. Pastor, M. Valtiner and J. Kunze-Liebhäuser, *Angew. Chem., Int. Ed.*, 2025, **64**, e202500965.
25 L. Deng, S.-F. Hung, Z.-Y. Lin, Y. Zhang, C. Zhang, Y. Hao, S. Liu, C.-H. Kuo, H.-Y. Chen, J. Peng, J. Wang and S. Peng, *Adv. Mater.*, 2023, **35**, 2305939.
26 S. Gong, B. Ni, X. He, J. Wang, K. Jiang, D. Wu, Y. Min, H. Li and Z. Chen, *Energy Environ. Sci.*, 2023, **16**, 5956–5969.
27 C. Ai, F. Dang, J. Wan, Z. Jiang, Y. Wu, J. Liu, H. Xu, Y. Wang, Y. Jian, M. Tian, C. Chen, Y. Yu and C. He, *ACS Catal.*, 2025, **15**, 7217–7231.
28 X. He, S. Xue, X. Liu, D. Xiong, X. Xiao, D. Wu, J. Wang, Q. Xu and Z. Chen, *Adv. Energy Mater.*, 2025, **15**, 2405473.
29 M. Li, Y. Huang, Q. Luo and Y. Ji, *Phys. Chem. Chem. Phys.*, 2025, **27**, 3206–3216.
30 Z. Li, H. Yang, W. Cheng and L. Tian, *Chin. Chem. Lett.*, 2024, **35**, 109237.
31 S. Barwe, J. Weidner, S. Cychy, D. M. Morales, S. Dieckhöfer, D. Hiltrop, J. Masa, M. Muhler and W. Schuhmann, *Angew. Chem., Int. Ed.*, 2018, **57**, 11460–11464.
32 C. Wang, Z. Zhao, W. Cao, Y. Peng, M. Song and Y. Wu, *Adv. Funct. Mater.*, 2025, **35**, 2502618.
33 H. Zhou, Y. Ren, B. Yao, Z. Li, M. Xu, L. Ma, X. Kong, L. Zheng, M. Shao and H. Duan, *Nat. Commun.*, 2023, **14**, 5621.
34 G. Liu, T. Nie, Z. Song, X. Sun, T. Shen, S. Bai, L. Zheng and Y.-F. Song, *Angew. Chem., Int. Ed.*, 2023, **135**, e202311696.
35 Y. Wan, Y. Tang, Y. Zuo, K. Sun, Z. Zhuang, Y. Zheng, W. Yan, J. Zhang and R. Lv, *Energy Environ. Sci.*, 2025, **18**, 7460–7469.
36 L. Deng, H. Chen, S.-F. Hung, Y. Zhang, H. Yu, H.-Y. Chen, L. Li and S. Peng, *J. Am. Chem. Soc.*, 2024, **146**, 35438–35448.
37 Y.-H. Wang, Y. Yang, F.-Y. Gao, X.-L. Zhang, L. Zhu, H.-K. Yan, P.-P. Yang and M.-R. Gao, *Angew. Chem., Int. Ed.*, 2024, **136**, e202407613.
38 H. Qin, Y. Ye, G. Lin, J. Zhang, W. Jia, W. Xia and L. Jiao, *ACS Catal.*, 2024, **14**, 16234–16244.
39 J. G. Davis, B. M. Rankin, K. P. Gierszal and D. Ben-Amotz, *Nat. Chem.*, 2013, **5**, 796–802.
40 R. Guo, Y. Zhou, W. Wang, Y. Zhai, X. Liu, W. He, W. Ou, R. Ding, H.-L. Zhang, M. Wu, Z. Jiang and K.-G. Zhou, *Sci. Adv.*, 2025, **11**, eadr5374.
41 X. Wang, S. Xi, W. S. V. Lee, P. Huang, P. Cui, L. Zhao, W. Hao, X. Zhao, Z. Wang, H. Wu, H. Wang, C. Diao, A. Borgna, Y. Du, Z. G. Yu, S. Pennycook and J. Xue, *Nat. Commun.*, 2020, **11**, 4647.
42 P. Ren, T. Gan, J. Cai, J. Hao, Z. Zhuang, C. Jin, W. Zhang, M. Du and H. Zhu, *Angew. Chem., Int. Ed.*, 2025, **64**, e202502776.
43 Z. Yang, F. Lai, Q. Mao, C. Liu, S. Peng, X. Liu and T. Zhang, *Adv. Mater.*, 2024, **37**, 2412950.
44 Q. Luo, K. Wang, Q. Zhang, W. Ding, R. Wang, L. Li, S. Peng, D. Ji and X. Qin, *Angew. Chem., Int. Ed.*, 2024, **137**, e202413369.
45 Z. Li, H. Liu, Y.-H. Wang, S. Ji, Y. Zhang, Y. Liu, X. Lu, H. Teng, J. H. Horton, Y. Wang, X. Ma and Y.-J. Tang, *ACS Nano*, 2024, **19**, 1600–1610.
46 Y. Ye, J. Xu, X. Li, Y. Jian, F. Xie, J. Chen, Y. Jin, X. Yu, M.-H. Lee, N. Wang, S. Sun and H. Meng, *Adv. Mater.*, 2024, **36**, 2312618.
47 J. Zhou, Y. Xiong, M. Sun, Z. Xu, Y. Wang, P. Lu, F. Liu, F. Hao, T. Feng, Y. Ma, J. Yin, C. Ye, B. Chen, S. Xi, Y. Zhu, B. Huang and Z. Fan, *Proc. Natl. Acad. Sci. U. S. A.*, 2023, **120**, e2311149120.
48 X. Yin, W. Sun, K. Chen, Z. Lu, J. Chen, P. Cai and Z. Wen, *Adv. Sci.*, 2024, **11**, 2402343.
49 Y. Niu, S. Gong, X. Liu, C. Xu, M. Xu, S.-G. Sun and Z. Chen, *eScience*, 2022, **2**, 546–556.